AGU PUBLICATIONS

JGR

Journal of Geophysical Research: Atmospheres

RESEARCH ARTICLE
10.1002/2016JD025993

Key Points:
- Shallow-to-deep convection transition and diurnal cycle of rainfall in the Central Amazon vary seasonally
- The transition of shallow-to-deep convection require a deeper moist layer during the dry and transition seasons than during the wet season
- Convective intensity is the strongest during the transition season due to high CAPE and CIN

Correspondence to:
Y. Zhuang,
zyz90@pku.edu.cn

Citation:
Zhuang, Y., R. Fu, J. A. Marengo, and H. Wang (2017), Seasonal variation of shallow-to-deep convection transition and its link to the environmental conditions over the Central Amazon, *J. Geophys. Res. Atmos.*, *122*, doi:10.1002/2016JD025993.

Received 7 OCT 2016
Accepted 18 JAN 2017
Accepted article online 22 JAN 2017

Seasonal variation of shallow-to-deep convection transition and its link to the environmental conditions over the Central Amazon

Yizhou Zhuang[1,2], Rong Fu[2,3], José A. Marengo[4], and Hongqing Wang[1]

[1]Department of Atmospheric and Oceanic Sciences, School of Physics, Peking University, Beijing, China, [2]Department of Geological Sciences, Jackson School of Geosciences, University of Texas at Austin, Austin, Texas, USA, [3]Department of Atmospheric and Oceanic Sciences, University of California, Los Angeles, Los Angeles, California, USA, [4]Centro Nacional de Monitoramento e Alertas de Desastres Naturais (CEMADEN), São Paulo, Brazil

Abstract This study aims to characterize the seasonal variation of the shallow-to-deep convection transition and understand how environmental conditions impact the behavior of this transition using data collected from the Observations and Modeling of the Green Ocean Amazon (GOAmazon) field campaign in the Central Amazon (Manaus). The diurnal cycle of the rain/cloud fraction shows that the wet season has more extensive shallow convection before the transition to deep convection with larger fractional coverage and rainfall; deep convection in the transition season is more intense and has higher vertical extension and a stronger updraft. Surface meteorology, atmospheric moisture, instability, and wind shear are contrasted for the shallow/congestus convection (SC) cases and the locally formed shallow-to-deep convection transition (LD) cases. The comparisons suggest that occurrence of the LD is generally promoted under the conditions of high atmospheric moisture and instability but has a weaker dependence on wind shear. The relative importance of these environmental controls also varies in different seasons: The dry and transition seasons require a deeper moist layer from the boundary layer to midtroposphere than the wet season; convective available potential energy (CAPE) is higher during the transition season, but it is a less important factor for shallow-to-deep convection transition than in other seasons; LD only has significantly larger wind shears than SC during the dry season.

1. Introduction

The Amazon region possesses about 50% of the global tropical rainforests [*Malhi and Grace*, 2000] and is well recognized as one of the major convective centers in the world [*Laurent et al*., 2002]. The rich rainforest canopy provides a considerable amount of surface evaporation, which in turn contributes to the frequent occurrence of tropical convection. A substantial amount of convective activity and precipitation takes place in the Amazon year round, but there are still some significant seasonal differences due to the annual variation of atmospheric circulation and the thermodynamic structure [*Marengo and Espinoza*, 2016; *Rao et al*., 1996]. *Fu et al*. [1999] provided the first comprehensive analysis of the atmospheric thermodynamic structure, its seasonal variations, and its influence on seasonal changes of rainfall over the Amazon using long-term radiosonde data at Manaus and Vilhena, atmospheric reanalysis data, and satellite data. They showed that the seasonal change of rainfall over the north central Amazon centered at Manaus can be best explained by the change of the convective inhibition energy (CIN). The change of CIN is mainly induced by humidity changes in the Atmospheric Boundary Layer (ABL) influenced by humidity entrained at the top of the ABL; in contrast, the changes of both convective available potential energy (CAPE) and CIN explain the seasonal change of rainfall over the southern Amazon centered at Vilhena. *Betts and Dias* [2010] noted that although water is normally sufficient throughout the year due to the deep rooting system of the extensive rainforest, regional scale subsidence in the dry season could significantly reduce cloud and increase solar radiation. The latter increases photosynthesis and thus evapotranspiration (ET), at surface. However, the increase of surface solar radiation also increases sensible flux which deepens daytime ABL. The deepening of the daytime ABL could reduce humidity in the ABL, even in the case of higher ET during the dry season [*Fu et al*., 1999]. *Machado et al*. [2004] found that dry season convection generally shows features of less precipitation, smaller low and high cloud cover, and fewer rain events. Previous studies [*Dias et al*., 2002; *Petersen et al*., 2006; *Petersen et al*., 2002; *Rickenbach et al*., 2002] also showed that convective systems over the Amazon vary between the "continental" type, referred to as the very deep convective systems (reaching 12–16 km

above the surface) with a large fraction of heavy rain rate from convective cores and active lightning activities and the "maritime" type, referred to as the relatively shallower deep convection (reaching 5–6 km above the surface) with a large fraction of medium rain rate from stratiform anvils without lightning. The changes between these two convective types are related to changes of CAPE, CIN, and vertical wind shear. *Kodama et al*. [2015] observed that the "continental" convective types are widespread 1 or 2 months before the onset of wet season, whereas "maritime" convective types become more prevalent during the wet season. This result is consistent with *Williams et al*. [2002] which showed that the dry-to-wet transition season rather than the wet season has a more unstable atmosphere which leads to the development of more intense deep convection in the southern Amazon.

Tropical convection, such as what occurs in the Amazon, is a key process in the climate system. It plays an important role in regulating the balance of water and energy, and it also helps to fuel the Hadley and Walker circulations [*Foley et al*., 2007]. However, global climate models show large uncertainties over the Amazon in reproducing observed rainfall variability and projecting rainfall patterns [*Li et al*., 2006; *Vera et al*., 2006; *Yin et al*., 2013]. Discrepancies in Amazon rainfall projections are a main source of uncertainty in projecting changes in global atmospheric CO_2 concentration due to carbon climate feedbacks [*Friedlingstein et al*., 2006, 2014]. *Anber et al*. [2015] also pointed out that representation of tropical convection in global climate models still remains unclear, and most modern climate models still fail to capture key features of tropical convection. The main issues are due to precipitation underestimation, an incorrect diurnal cycle of precipitation intensity, etc. These problems are linked to the inability to simulate a smooth shallow-to-deep convection transition. Shallow and deep convection are often parameterized separately in climate models, and the parameterization of deep convection usually utilizes large-scale atmospheric features, such as CAPE, to determine the onset and intensity of the convection [*Zhang and Mcfarlane*, 1995]. The shallow-to-deep convection transition has been studied extensively over tropical oceans [*Del Genio et al*., 2012; *Hagos et al*., 2014; *Rowe and Houze*, 2015; *Ruppert*, 2016; *Ruppert and Johnson*, 2016; *Xu and Rutledge*, 2016] and over land [*Khairoutdinov and Randall*, 2006; *Zhang and Klein*, 2010] using cloud resolving models and research quality data provided by field campaigns, particularly by the U.S. Department of Energy (DOE) Atmospheric Research Measurement (ARM) [*Ackerman and Stokes*, 2003; *Stokes and Schwartz*, 1994]. However, a systematical characterization of the shallow-to-deep convection transition, its influence on convective intensity and rain rate, and its relationship with the ambient atmospheric thermodynamic and dynamic structures during the wet, dry, and dry-to-wet transition seasons, respectively, over the Amazon are not yet available in literature.

In this paper, we evaluate how environmental conditions influence the transition from shallow to deep convection and the diurnal cycle of rainfall during different seasons by analyzing observational data provided by the Observations and Modeling of the Green Ocean Amazon (GOAmazon) field campaign led by the DOE ARM Mobile Facility [*Martin et al*., 2016] and Brazil's CHUVA Project [*Machado et al*., 2014]. The data used in this study are introduced in section 2. The methods for classifying seasons and convective regimes are described in section 3. Section 4 gives an overview of general features of the shallow-to-deep convection transition in terms of the diurnal cycle of rain/cloud fraction and the rain rate. Section 5 analyzes the environmental controls on the shallow-to-deep convection transition. Main conclusions are summarized and discussed in Section 6.

2. Data

2.1. GOAmazon Experiment

The GOAmazon and CHUVA field campaign experiment data were retrieved from the ARM archive (http://www.archive.arm.gov). All observation data in this study were measured at the T3 site (3.21°S, 60.60°W) in Manacapuru, except for the S band radar which was measured approximately 70 km to the east at the T1 site (3.15°S, 59.99°W) in Manaus. Detailed information for each specific data set is listed below:

2.1.1. S Band Radar Reflectivity

Equivalent radar reflectivity factor data (Z) was obtained from the Sistema de Proteção da Amazônia (SIPAM) ground-based S band (10 cm wavelength), Doppler, single-polarization radar located in Manaus. The S band radar, with a horizontal beam width of 0.96° and a vertical beam width of 0.93° routinely performs a volume

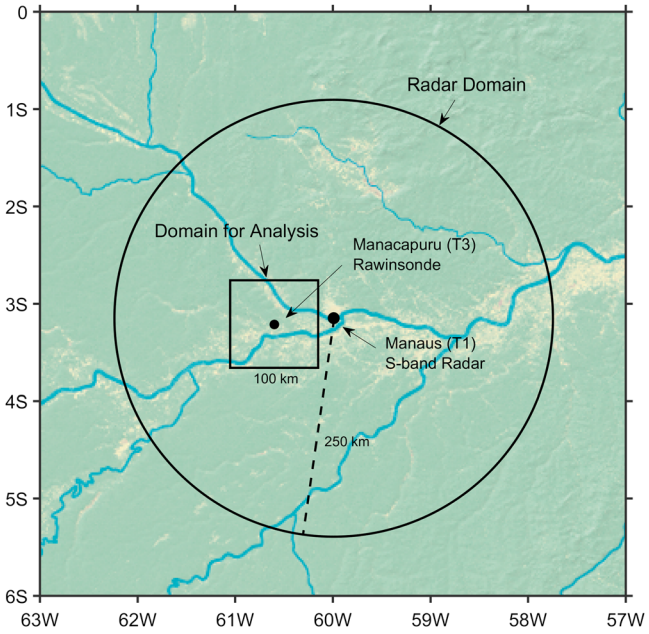

Figure 1. Location of the S band radar and other instruments.

scan. This contains multiple Plan Position Indicator (PPI) scans at up to 17 elevation angles from 0.9° to 19°, every 12 min. The reflectivity products we use are processed by Courtney Schumacher and are already interpolated to the Constant Altitude Plan Position Indicator (CAPPI) data with a horizontal resolution of 2 km and a vertical resolution of 0.5 km (altitude ranges from 0.5 to 20 km). The reflectivity data are also corrected for gas attenuation and ground clutter. In order to match the geographical representation of other data sets retrieved from the T3 site, only data within a 100 km grid box centered at the T3 site are used in this study (see Figure 1). The radar data are available from January 2014 to August 2015 (there is also a large data gap in November 2014). This data set is imperfect in some ways: there are data gaps at certain times and at high-elevation angles; clear air returns, which are mostly below 20 dBZ at night for low elevation, are significant in some time periods and not yet removed.

The 20 dBZ and 40 dBZ rain fractions, defined as fractional coverage of $Z \geq 20$ dBZ representing the area of convective systems and $Z \geq 40$ dBZ representing the area of intense precipitation or a convective core in the 100 km grid box, are calculated for each level. Rain rate is also computed using the reflectivity (mm^6/m^3) field at 2.5 km altitude and the *Z-R* relation $Z = 139\ R^{1.43}$ derived by *Tokay and Short* [1996]. These Z-R relations were also used to derive rain rate over Amazon in previous study which used the same radar [*Cohen et al.*, 2014]. But this simple rain rate derivation method still has certain limitations as the drop size distribution could also vary seasonally due to different aerosol conditions.

2.1.2. Active Remote Sensing of Clouds (ARSCL) Cloud Mask

The vertical profile of the cloud mask is retrieved from W band ARM Cloud Radar Active Remote Sensing of Clouds (WACR-ARSCL) data (available at https://www.arm.gov/data/vaps/wacrarscl/arsclwacr1kollias). This product is derived from combined observations from the 95 GHz W band ARM Cloud Radar (WACR), Micropulse Lidar (MPL), and ceilometer using the new WACR-ARSCL VAP algorithm [*Kollias et al.*, 2007]. This product is available from mid-February 2014 to November 2015. Cloud fraction, defined as temporally fractional coverage every 12 min, is calculated at each level for further analysis.

2.1.3. Rawinsonde Profile

There are 2824 available rawinsonde profiles in total from the T3 site (available at https://www.arm.gov/data/datastreams/sondewnpn). The rawinsondes were regularly launched 4 times per day at about 02, 08, 14, 20 Local Standard Time (LST, 4 h behind UTC). During two Intense Observation Periods of the GOAmazon experiment in 2014 (February–March and late August–October), additional rawinsondes were launched at about 11 LST, making it 5 times per day. Available variables from the rawinsonde data include dry-bulb temperature (T), dew point temperature (T_d), relative humidity (RH), atmospheric pressure (p), eastward wind speed (u), and northward wind speed (v).

All rawinsonde profile data were regridded onto a constant altitude grid starting from 100 m (50 m above the surface) to 16 km above sea level with a 100 m interval. Specific humidity (q), potential temperature (θ), equivalent potential temperature (θ_e), saturation equivalent potential temperature (θ_{se}), CAPE, and CIN are also computed using the original variables. The parcels with mean temperature and humidity of the 500 m mixing layer are used in the calculation of CAPE and CIN.

2.1.4. The 1290 MHz Radar Wind Profiler

The horizontal wind profile is from the radar wind profiler which operates at 1290 MHz (available at https://www.arm.gov/data/datastreams/1290rwpwindcon). It has two power levels: at low power level, it measures the wind profile between 120 m and 2.5 km with 60 m resolution; at high power level, it measures the wind profile up to ~6 km but with lower vertical resolution (~200 m).

2.1.5. Other Surface Measurements

Surface air temperature, relative humidity, pressure, rain rate, wind speed, and wind direction are from the Surface Meteorological System (MET) (available at https://www.arm.gov/instruments/met).

Precipitable Water Vapor (PWV) is from the MicroWave Radiometer (MWR) (available at https://www.arm.gov/data/vaps/mwrret/mwrret1liljclou).

Surface upward/downward shortwave/longwave hemispheric radiance is from the Ground Radiation (GNDRAD) collection of radiometers (available at https://www.arm.gov/data/vaps/qcrad/qcrad1long).

Surface sensible and latent heat flux are from the Eddy CORrelation (ECOR) flux measurement system (available at https://www.arm.gov/data/vaps/qcecor/30qcecor).

2.2. The European Centre for Medium Range Weather Forecast Diagnostic Analyses

The European Centre for Medium Range Weather Forecast Diagnostic Analyses (ECMWF-DIAG) data are diagnostic products of real time simulations from ECMWF model runs at specific ARM locations or for area averages (interpolated to T3 site at a $0.56° \times 0.56°$ grid here) [*European Centre for Medium Range Weather Forecast*, 1994]. Two kinds of data streams are retrieved: ECMWFSFC1L and ECMWFVAR (available at https://www.arm.gov/capabilities/instruments/ecmwfdiag) where the temporal intervals of both are 1 h. ECMWFSFC1L provides surface variables and fluxes among which precipitation rate (P), surface sensible heat flux (H), latent heat flux (LE), surface shortwave net radiative flux (F_{SW}), and longwave net radiative flux (F_{LW}) are used in this study. ECMWFVAR provides model meteorological and cloud variables at 137 vertical levels among which specific humidity (q) is used in this study.

PWV can be calculated by $\mathrm{PWV} = \frac{1}{\rho_w g}\int_{1000\ \mathrm{hPa}}^{100\ \mathrm{hPa}} q\,dp$, where $\rho_w = 10^3$ kg/m^3 is the density of water, $g = 9.8$ m/s^2 is the acceleration of gravity, and p is the pressure of each vertical level. To investigate the potential impact of moisture transport due to large-scale motion, the vertical integral of the moisture flux convergence (MFC) is then computed from $\frac{\partial \mathrm{PWV}}{\partial t} = \mathrm{MFC} + E - P$, where $E = \frac{\mathrm{LE}}{\rho_w L_v}$ is the evaporation rate and $L_v = 2.5 \times 10^6$ J/kg is the latent heat of vaporization [*Wei et al.*, 2016]. The MFC can also be written as $\mathrm{MFC} = -\int_{1000\mathrm{hPa}}^{100\mathrm{hPa}} \nabla\cdot(q\rightarrow V)\,dp$. The diurnally accumulated MFC is defined as $\int_{00\ \mathrm{LST}}^{t} \mathrm{MFC(t)}\ dt$.

3. Convective Regime Classification

Monthly precipitation derived from S band radar CAPPI at an altitude of 2.5 km (100 km grid mean) and from ECMWF-DIAG are shown in Figure 2. Although precipitation values from these two sources do not match well for every month, their annual trends are in general agreement with one another. For the following analysis, all 12 months are divided into three seasons for composite: (1) Wet season: January–May; (2) Dry season: June–September; (3) Dry-to-Wet Transition (Trans) season: October–December. The wet season definition matches with most previous studies at Manaus [*Marengo et al.*, 2013; *Yin et al.*, 2013]. However, the dry and transition seasons are slightly different from previous studies. *Yin et al.* [2013] defines the dry and transition seasons as JJA and SON, respectively.

In order to study the shallow-to-deep convection transition, we evaluate the diurnal cycles of both rain fraction from S band radar and cloud fraction from the ARSCL cloud mask product. The ARSCL cloud mask product is derived from vertical pointing remote sensing measurements. It has the capability to capture nonprecipitating shallow convection, as well as high cloud such as cirrus and convective anvil, but its horizontal representation is only at a single point. On the other hand, the S band radar rain fraction has a better horizontal representation but could miss some shallow or small-size convection. Also, neither of these two data sets fully cover the year of 2014 and 2015. Therefore, by utilizing the combination of ARSCL cloud fraction and S band radar rain fraction defined in section 2.1.2, we can have a better view on the shallow-to-deep convection transition and gain more samples than from using a single data set.

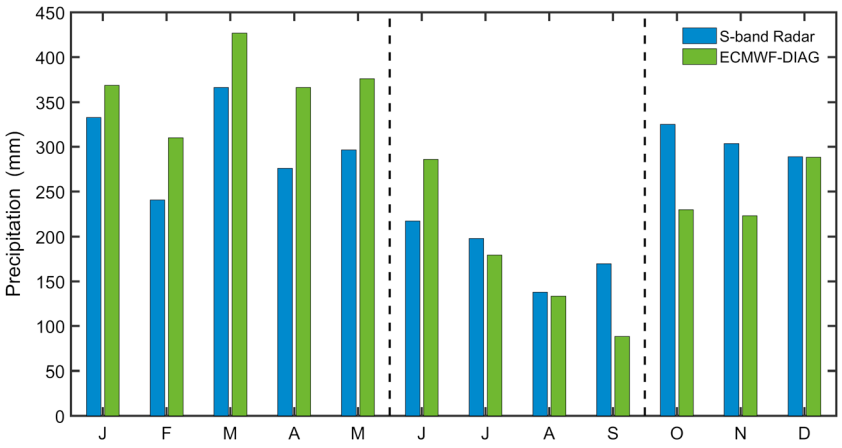

Figure 2. Monthly accumulated precipitation averaged for 2014 and 2015.

Thresholds for cloud fraction and 20 dBZ rain fraction are first determined manually (0.2 and 0.02) before making a classification for the samples. Two types of convective regimes are defined as below, and their requirements are listed (both two should be met):

1. Shallow and congestus convection day (SC)/nontransition case: (1) No cloud and rain fraction is above 6 km between 08 and 18 LST; (2) cloud or rain fraction below 6 km lasts for more than 1 h between 08 and 18 LST.
2. Locally formed daytime deep convection day (LD) / transition case: (1) Cloud or rain fraction above 8 km occurs at any time between 08 and 18 LST, and the cloud base is below 2 km; (2) no cloud and rain fraction above 6 km occurs before 06 LST.

The above criteria for day selection is first performed automatically by the computer program. The thresholds for the cloud and rain fraction are determined empirically. Slight adjustment of these thresholds would change the sample number for SC and LD cases, but it will not change the composite results much for the following analysis. Manual inspection of radar images and the cloud/rain fraction diurnal cycle is then applied to the initial classification results to make corrections and eliminate cases linked to fast-moving Mesoscale Convective System (MCS) which are already mature before passing the T3 site. Manual inspection of S band radar images suggests that there are 61 of 400 LD cases linked to fast-moving MCS.

The classified categories are similar to those defined by *Zhang and Klein* [2010]. Rather than using precipitation rate to determine various convective regimes similar to the U.S. Southern Great Plains (SGP) site, we select cases using cloud and rain fraction with a certain height extension. The advantage of using the cloud/rain fraction is that the classification results will have less uncertainty compared to only using precipitation rate derived from single-level radar reflectivity or other single-point ground observations.

In this study, we are more concerned with the shallow-to-deep convection transition and the environmental conditions that determine whether the shallow convection can or cannot develop into deep convection. Previous satellite imagery analysis showed that there are three major precipitation modes in the Amazon: the Coastal Occurring System (COS), the Basin Occurring System (BOS), and the Locally Occurring System (LOS); each can have a very distinctive triggering mechanism and influence on the environment [*Greco et al*., 1990]. Therefore, in order to make sure that only locally generated daytime deep convection is present in our LD cases, we manually went over all radar composite reflectivity animation. We then removed cases in which convection was already fully organized and at its mature phase at least 2 h before passing through T3 site; these cases were generally linked to a very large MCS, such as a squall line. The final classification result showed that there are 56, 121, and 50 days for SC cases in the wet, dry, and transition seasons, respectively, and 134, 65, and 40 days for LD cases.

4. Overview of Shallow-to-Deep Convection Transition and Rainfall Diurnal Cycle

Figures 3 and 4 show the diurnal cycle of the composite rain fraction derived from S band radar reflectivity and cloud fraction derived from the ARSCL cloud mask, respectively. In order to better illustrate

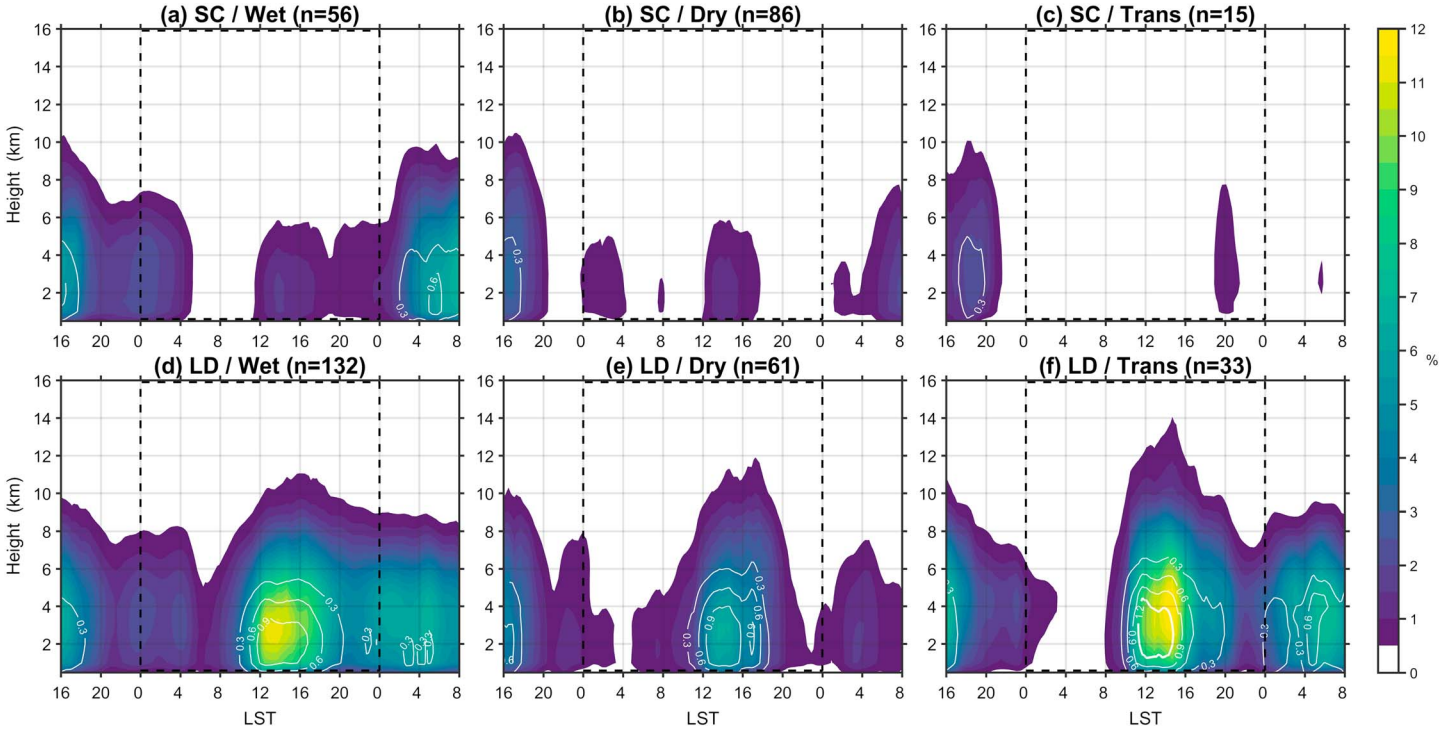

Figure 3. Composite diurnal cycle of rain fraction computed from S band radar reflectivity data in SC and LD days in different seasons. Colors represent 20 dBZ rain fraction and contours represent 40 dBZ rain fraction.

continuous changes of convection development, fractions from the previous and following days are also partially covered (outside of the black dashed rectangle in each subfigure).

Figures 3a–3c show that the daytime shallow convection develops after 12 LST in SC days, where the maximum rain fraction never exceeds 2%. The wet season has the largest shallow convection fraction, while the transition season has the smallest. For LD days (Figures 3d–3f), rain fraction in the lower troposphere is 4–10 times higher than that for SC days. Convective systems reach their maximum sizes in the early afternoon. Note that rain fraction below ~2 km could be underestimated since the radar beam cannot cover the whole grid box at that altitude. In LD days during the wet season, the 20 dBZ rain fraction in the lower troposphere is larger, peaks earlier (~13 LST), and persists longer than the other two seasons; the 40 dBZ rain fraction (contour line) also suggests that there is a broader temporal coverage of intense rainfall. During the dry season, the 20 dBZ rain fraction is much smaller and has a shorter time period than wet season. However, the maximum 40 dBZ rain fraction has similar maximum value in the wet season but persists shorter, indicating that dry season deep convection generally has a smaller fractional coverage and lasts shorter but could have a larger instantaneous rain rate. During the transition season, the 20 dBZ rain fraction below 3 km in the afternoon is approximately the same (only a little smaller) as in the wet season, while that above 3 km is larger, peaks later, and has a higher vertical extension than the wet season. This suggests that the transition season develops the deeper convection possibly with a stronger updraft. The largest value in the 40 dBZ rain fraction also indicates that the transition season develops the most intense rainfall. These seasonal variations of LD systems are broadly consistent with previous findings that showed that the increase of "maritime" convection contributes to more rainfall during the wet season, whereas "continental" convection produces much of the rainfall during the dry and transition seasons [*Betts et al*., 2009; *Williams et al*., 2002].

In Figure 3, deep convection development is well depicted, but shallow convection and some high cloud echoes like anvils are hard to capture using the S band radar due to its long wavelength and elevation angle limit of PPI scan. The cloud fraction in Figure 4 can overcome this disadvantage, but has other limitations. Because the cloud fraction is derived from vertical pointing remote sensing measurements, its spatial representation is not as good as the rain fraction derived from the scanning S band radar (one single point rather than a 100 km grid box). In SC days, shallow convection in the boundary layer usually initiates after 09 LST and

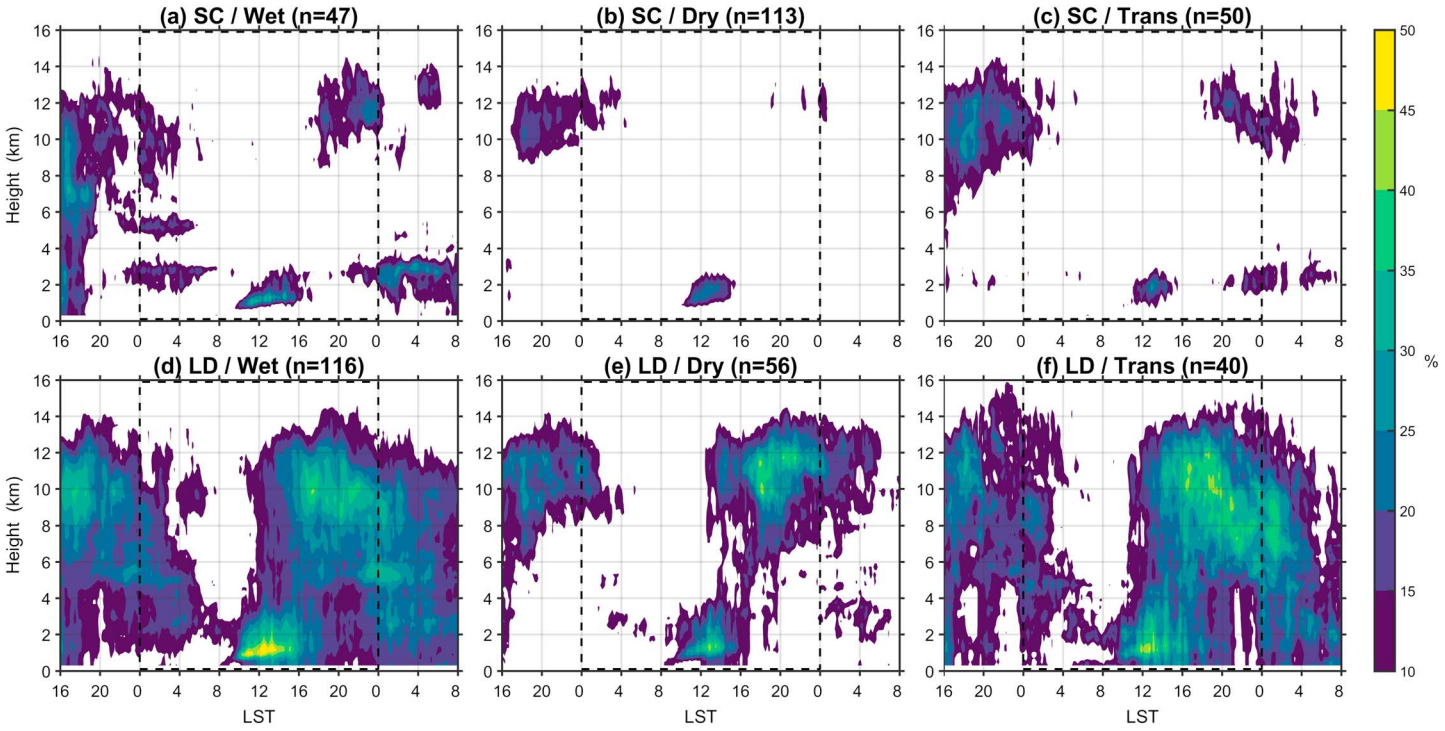

Figure 4. Composite diurnal cycle of cloud fraction calculated from the ARSCL cloud mask product in SC and LD days in different seasons.

dissipates before 16 LST with the wet season developing shallow convection with the longest lifetime and the transition season having the shortest lifetime (initiates later and ends earlier). Fractional coverage of shallow convection during the wet season is the greatest, while that in the transition season is the least in SC days; this is consistent with rain fraction in Figure 3. In LD days, deep convection in the middle to upper troposphere cannot be fully seen due to significant beam attenuation, yet the shallow-to-deep convection transition and the anvil in the upper troposphere are shown more clearly. Compared to SC days, LD develops from shallow convection occurring during late morning to early afternoon with a lower cloud base. Also, the wet season has the most extensive shallow convection prior to the development into deep convection. The dry season has the least fractional coverage of shallow convection, and the transition to deep convection seems to occur a little later than that for the other two seasons; the transition season develops deep convection with most extensive anvils.

The three seasons also show different modes of the rain rate diurnal cycle. Figure 5 shows the composite diurnal cycle of radar-derived rain rate for LD cases in the different seasons. The transition season shows largest peak rain rate but also has biggest variation, while the peak rain rate in the dry season is the smallest. The mean rain rate during the wet and transition seasons peaks at ~12–13 LST and ~1 h later during the dry season. We can also see that the peak time of rain rate does not match well with that of the rain fraction in Figure 3. The mean rain rate in a grid box is proportional to the rain fraction at the low level only if the rain rate field is homogenous and constant. However, this is hardly the case; the diurnal cycles of the rain fraction and rain rate do not resemble each other completely. Rain fraction in the lower troposphere (Figure 3) seems to peak ~1–3 h later in the early afternoon than the rain rate in LD days during the wet and transition seasons. This is possibly due to deep convection in these seasons tending to grow larger stratiform rainfall that contributes to a larger rain fraction, as shown in Figure 4.

5. Environmental Conditions Influencing the Shallow-to-Deep Transition

In order to infer what environmental conditions favor the transition from shallow to deep convection and how deep convection likely changes the conditions, surface and boundary layer thermodynamics, atmospheric moisture, instability, and wind shear conditions are contrasted between SC and LD days and

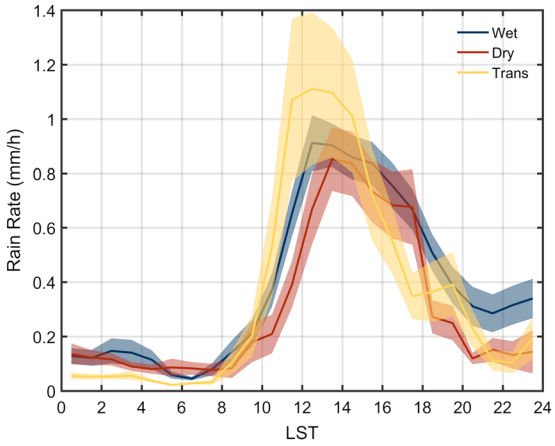

Figure 5. Composite diurnal cycle of radar-derived rain rate for LD days. Shaded regions represent 1 standard error.

described in the form of the diurnal cycle. The error bar and shaded region in the figures represent 1 standard error.

5.1. Surface Meteorology

Figure 6 shows the diurnal cycle of net shortwave (F_{SW}), net longwave (F_{LW}), and net total ($F_{net} = F_{SW} + F_{LW}$) radiative flux in SC and LD days during the three different seasons. Data from radiometers and ECMWF-DIAG are both plotted for comparison and to reduce uncertainty in our conclusions. There are differences in the flux value between the two data sets. In particular, F_{SW} of the ECMWF-DIAG is ~100 W/m^2 higher than that of the radiometer, whereas F_{LW} from the ECMWF-DIAG is ~40 W/m^2 weaker than that of the radiometer during the daytime. Assuming the radiometer observation have relatively accurate representation of the radiative flux with small error, these discrepancies between the observations and model results indicate that the ECMWF model may underestimate cloud amount and lead to larger F_{SW}, and the smaller upward F_{LW} in ECMWF-DIAG could be a result of overestimation of water vapor amount in the atmosphere. Nevertheless, the patterns between SC/LD differences and seasonal variations from the two data sets are mostly similar. Due to a smaller cloud/rain fraction, SC days have larger F_{SW} during the daytime than LD days. Similarly, for LD days, but during different seasons, the dry and transition seasons also show larger solar heating than the wet season. Note that sunrise occurs at ~06 LST during the wet and dry seasons and is ~20 min earlier during the transition season. This means that morning F_{SW} increases a little earlier during the transition season. On the other hand, F_{LW} is closely linked to the surface temperature, water vapor content in the atmosphere, and cloud cover. Therefore, the larger upward F_{LW}

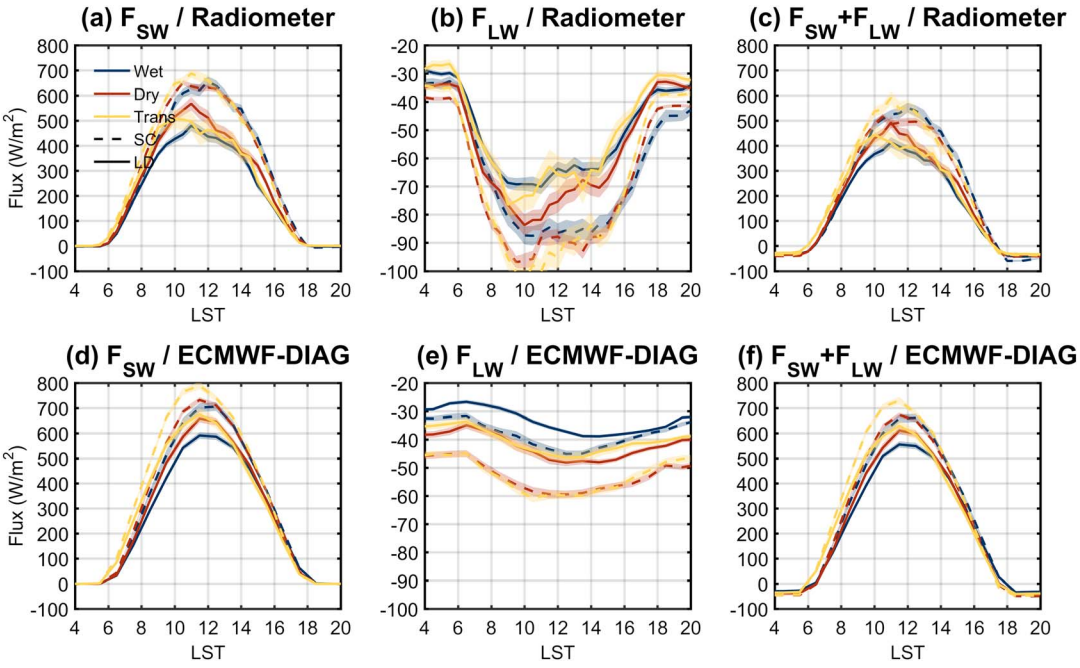

Figure 6. Composite diurnal cycle of shortwave and longwave radiative flux in SC and LD days in each season. Shaded regions represent 1 standard error.

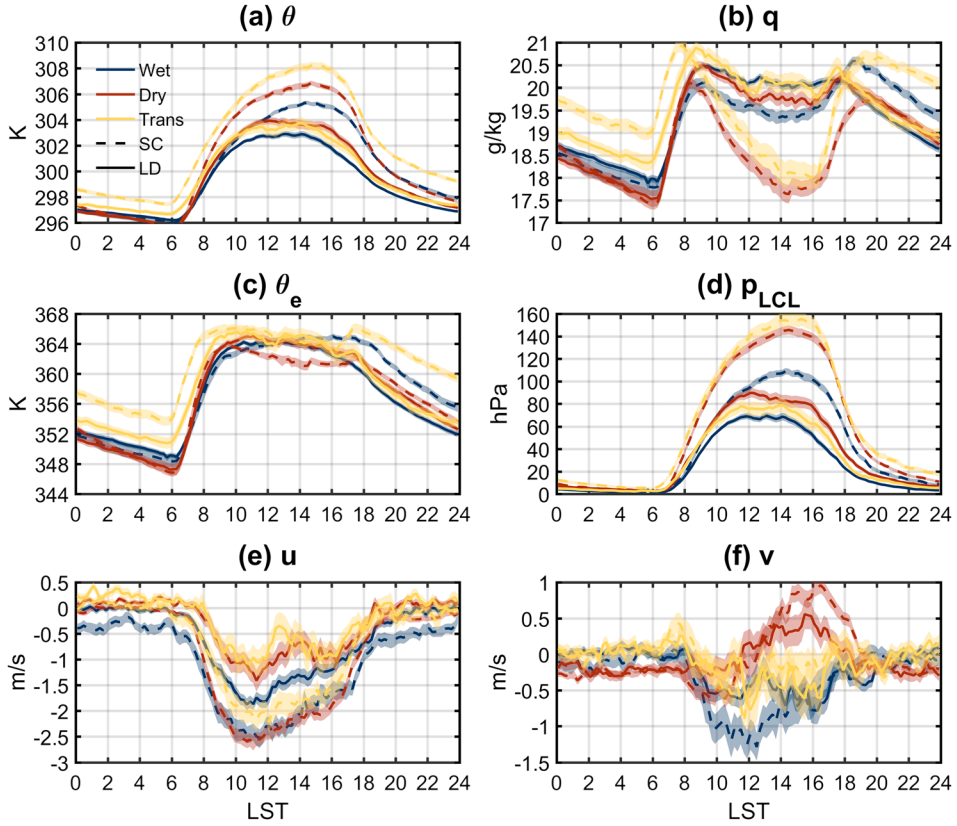

Figure 7. Composite diurnal cycle of surface parameters θ, q, θ_e, p_{LCL}, and wind (u, v) in SC and LD days during each season. Shaded regions represent 1 standard error.

during SC days, especially during the dry and transition seasons, is consistent with higher surface temperatures, a less humid atmosphere, and smaller cloud cover associated with shallow convection.

Diurnal cycles of surface thermodynamic parameters are displayed in Figure 7 including: potential temperature (θ), specific humidity (q), equivalent potential temperature (θ_e), and p_{LCL} [*Betts et al.*, 2002]. The surface thermodynamic diurnal cycles are mostly driven by radiative forcing, so the patterns in Figure 7 somewhat resemble those in Figure 6.

The surface potential temperature θ in Figure 7a shows a typical diurnal cycle pattern similar to other continental regions [*Collow et al.*, 2016], but differences exist between both SC and LD days and between different seasons. The parameter θ reaches its minimum immediately before sunrise, then quickly rises and peaks at 12–14 LST and 14–15 LST in LD and SC days, respectively. The difference between minimum θ for SC and LD days is very small ($<$0.2 K during the wet and dry seasons and $<$1 K during the transition season). However, maximum θ for SC days is significantly higher than that for LD days (about 2, 3, and 4 K for the wet, dry, and transition seasons, respectively). As for seasonal variation, θ has the smallest values and variability during the wet season. Conversely, θ has the largest values for LD days during the dry season and the largest values for SC days during the transition season. These differences in the θ value, the θ range, and the θ peak time can be accounted for by the differences in cloud cover and surface solar heating.

Immediately before sunrise, the minimum surface specific humidity q is reached because colder air holds less water vapor (T/q_s also reaches minimum). After sunrise, q quickly rises as temperature increases and dew evaporates. After ~08 LST, q decreases since shallow convection brings up moisture, and drier tropospheric air is entrained into the ABL as the daytime ABL deepens. In LD days, as precipitation proceeds, upward moisture flux is balanced by evaporation of precipitation, so q does not change much during 12–16 LST in LD days; however, in SC days, q still keeps dropping and reaches a second minimum at 14–15 LST, especially during the dry and transition seasons. After the late afternoon, q rises back as dry air entrainment into the boundary layer weakens. Difference of q between LD and SC days during the daytime is much smaller during the wet

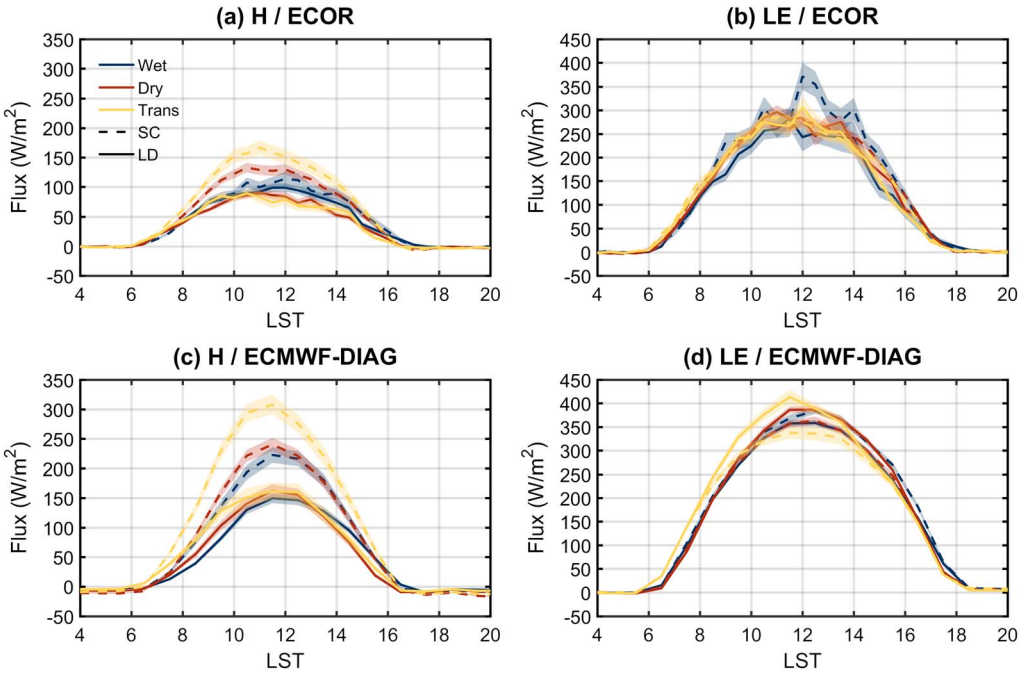

Figure 8. Composite diurnal cycle of surface-sensible and latent heat flux from ECOR and ECMWF-DIAG in SC and LD days during each season. Shaded regions represent 1 standard error.

season than during the other seasons as more frequent convection happens during the wet season, and the deep rooting system and high photosynthesis/evapotranspiration can help remain similar q in the ABL [*Gash and Nobre*, 1997].

The equivalent potential temperature θ_e is an important parameter that is conserved during a reversible wet adiabatic process. The diurnal cycle of θ_e is the combined result of θ and q. Surface θ_e for LD days is 1–3 K higher during the dry seasons than for SC days at 10–17 LST which reflects significantly higher water vapor in LD days; during the wet and transition season, the θ_e difference between SC and LD days is insignificant as the difference of θ and that of q cancel each other. After late afternoon, θ_e decreases faster in LD days than in SC days as convective downdrafts bring down air with low θ_e to the mixed layer, especially during the wet season, in which there is more extensive deep convection.

The p_{LCL}, which denotes the pressure height from the surface to the cloud base level, is calculated from the surface temperature and RH using the formula given by *Betts et al*. [2002]. The p_{LCL} is also a good estimate of the mixed layer height over land when ABL clouds occur during the daytime [*Betts*, 2009]. The p_{LCL} is closely linked to surface temperature and humidity shown in Figures 7a and 7b. Incoming shortwave radiative flux F_{SW} can increase surface temperature, thus heat up the ABL and lead to the increase of p_{LCL}. On the other hand, rainfall evaporation will increase humidity and bring the ABL closer to saturation, resulting in the decrease of p_{LCL}. In Figure 7d, it can be seen that the mixed layer in SC days deepens faster than that in LD days. This is because extensive cloud cover, strong convective updrafts, and heavy precipitation in LD days could slow down the warming and growth of the daytime mixed layer. The seasonal difference can also be accounted for by the same reason: the wet season LD days have a shallower mixed layer.

Surface winds u and v are very small at night due to decoupling between the surface and free tropospheric winds; this effect is weakened during daytime by convective mixing as surface temperature increases. During the daytime, northeasterly winds are dominant during the wet and transition seasons, and southeasterly winds dominate during the dry season. A comparison of SC and LD days shows that LD days have smaller surface wind speeds which is most pronounced during the dry season.

Similar to the radiative flux in Figure 6, Figure 8 shows the surface sensible and latent heat flux (H and LE) plotted using two data sets. Discrepancies between the two data sets are also present here: diurnal peak H from ECMWF-DIAG is significantly larger than that from ECOR observation, especially for SC cases. This

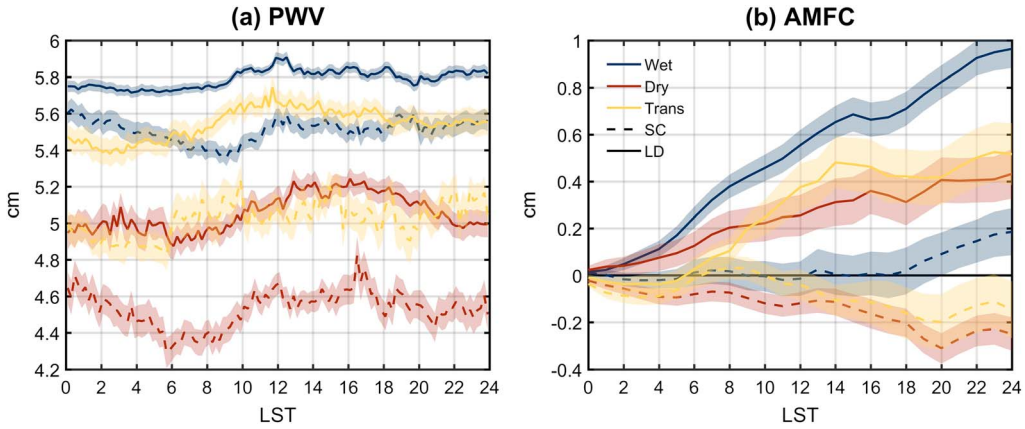

Figure 9. Diurnal cycle of PWV (MWR) and AMFC (ECMWF-DIAG) in SC and LD days in each season. Shaded regions represent 1 standard error.

again could indicate the overestimation of F_{SW} and surface temperature due to underestimation of cloud amount (especially the shallow clouds) in ECMWF-DIAG, which is discussed before when referring to Figure 6. Although ECMWF-DIAG sensible heat flux is about 50–130 W/m^2 higher than the ECOR measurement, it is still evident that SC days have a higher sensible heat flux than LD days, which is related to the stronger solar radiative heating. This relationship between deep convection and small sensible heat flux is similar to those found in the SGP and tropical oceans [*Sobel*, 2003; *Zhang and Klein*, 2010]. The seasonal variation in the sensible heat flux is similar to the solar radiation in Figure 6; the SC cases during the transition season has the largest flux due to the strongest solar heating and least cloud cover. Latent heat flux, on the other hand, is less distinguishable between SC and LD days as it is mostly dominated by

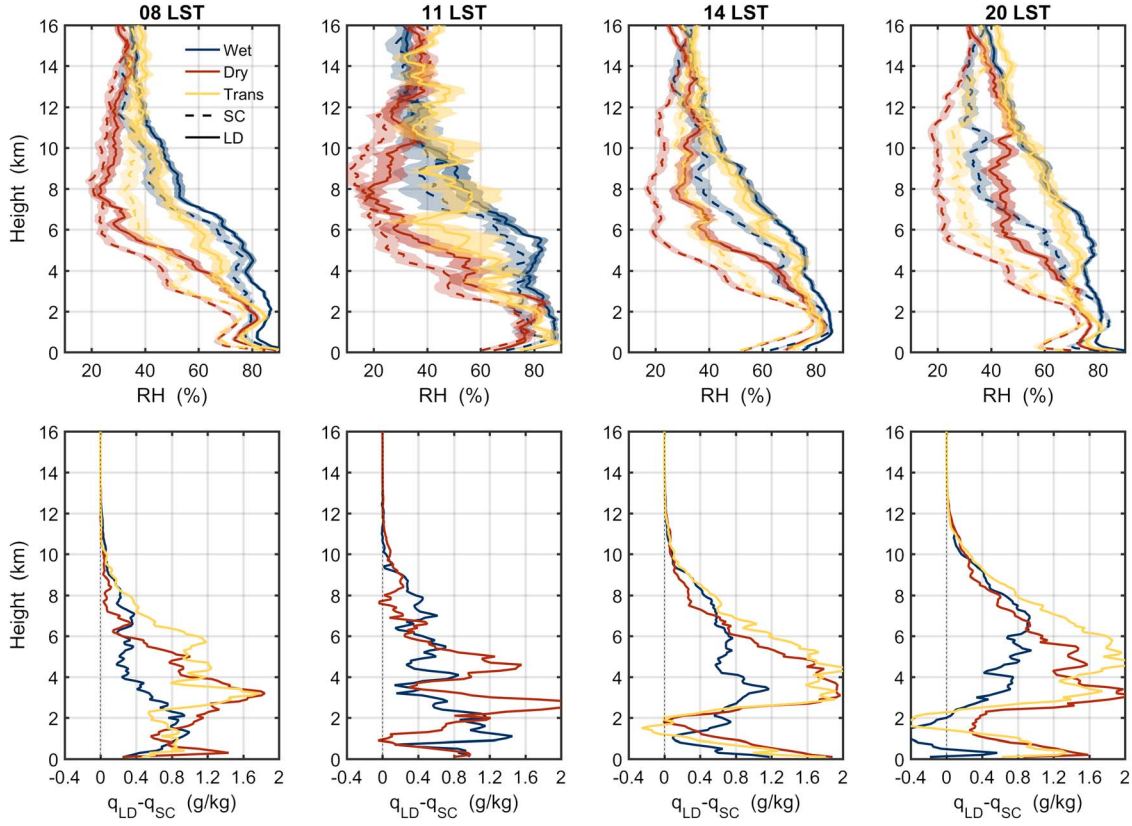

Figure 10. (top row) Composite RH profiles in SC/LD days and (bottom row) specific humidity difference profiles between LD and SC days at 08, 11, 14, and 20 LST in each season. Shaded regions (Figure 10, top row) represent 1 standard error.

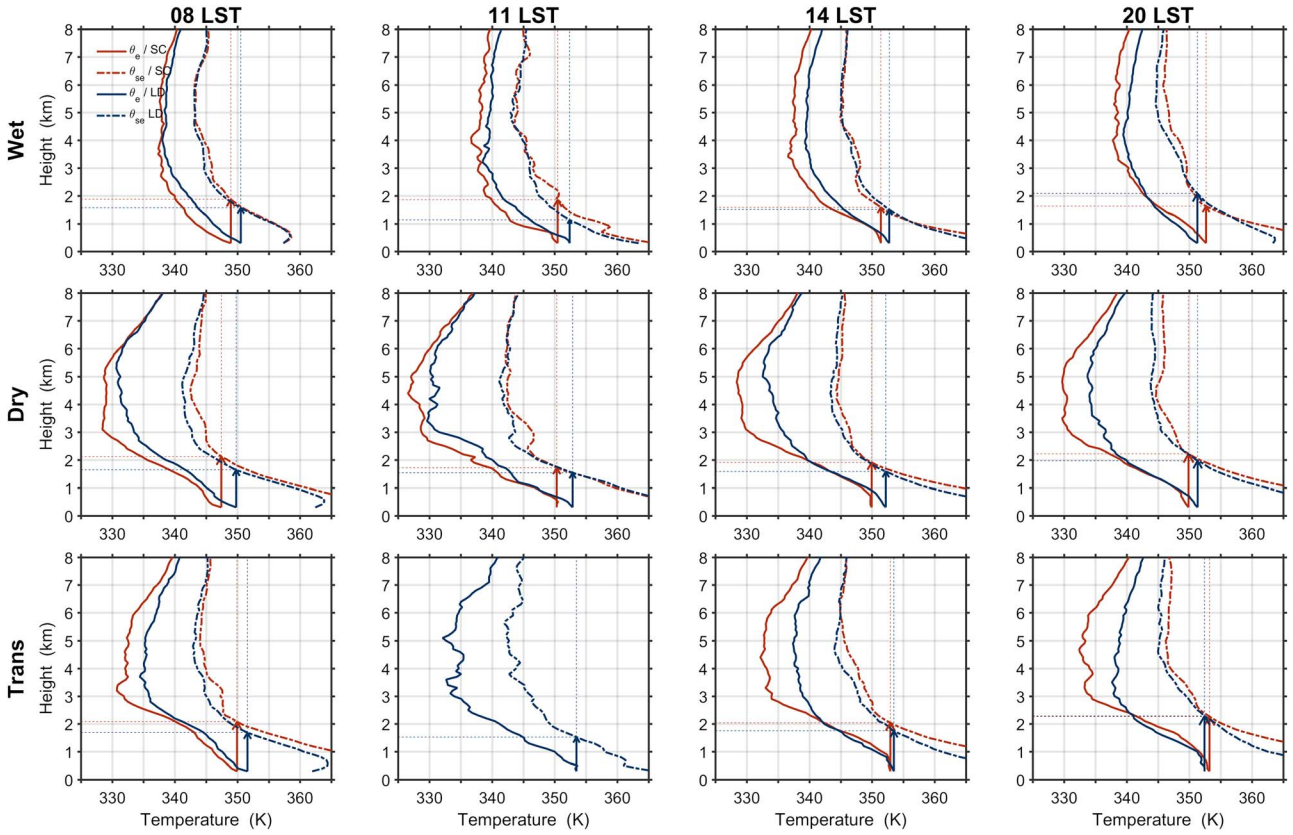

Figure 11. Composite equivalent potential temperature θ_e and saturation equivalent potential temperature θ_{se} profiles at 08, 11, 14, and 20 LST in SC and LD days during each season. Arrows indicate rising of air parcel with mean θ_e of the 500 m mixed layer.

high evaporation rates from the forest (canopy). Likewise, the seasonal difference in the latent heat flux is not very significant and is inconsistent between the two data sets.

5.2. Atmospheric Moisture

Figure 9 shows the diurnal cycles of PWV and diurnally accumulated MFC in SC and LD days during the three seasons derived from the MWR and ECMWF-DIAG data, respectively. Showing accumulated MFC instead of MFC is because the accumulated moistening effect could be more important than a value at a specific time for deep convection development, and it will be easier to make comparison between different seasons by using the accumulated value. PWV statistics indicates that the wet season has a larger average PWV (5.76 cm) but smaller variation ($\sigma = 0.33$ cm) compared to those during the dry season (PWV = 4.75 cm, $\sigma = 0.63$ cm) and the transition season (PWV = 5.34 cm, $\sigma = 0.50$ cm). Consequently, the PWV difference between the composite diurnal cycle for SC days and that for LD days is predominantly small during the wet season. However, during the dry and transition seasons, the environmental PWV is much higher for LD days than for SC days. The steady growth in diurnally accumulated MFC in LD during the three seasons signifies large continuous moisture convergence into the air column that results in a bigger PWV. In contrast, SC is associated with a diurnal accumulation of negative MFC caused by moisture divergence during the dry and transition seasons. However, moisture divergence during the wet season is not significant (diurnally accumulated MFC is close to 0), which is consistent with the smaller variation (standard deviation) of PWV during this season.

Figure 10 further shows composite relative humidity (RH) profiles in LD and SC days and the specific humidity difference ($q_{LD} - q_{SC}$) at 08, 11, 14, and 20 LST. During the wet season at 08 LST (before convection), LD days are slightly wetter (~10% in RH, 0.6 g/kg in q) than SC days below 4 km but do not show much difference at midtroposphere; as mixed layer deepens and deep convection develops, RH difference grows up to higher altitude, but it is not until 20 LST around the end of deep convection that the RH difference become

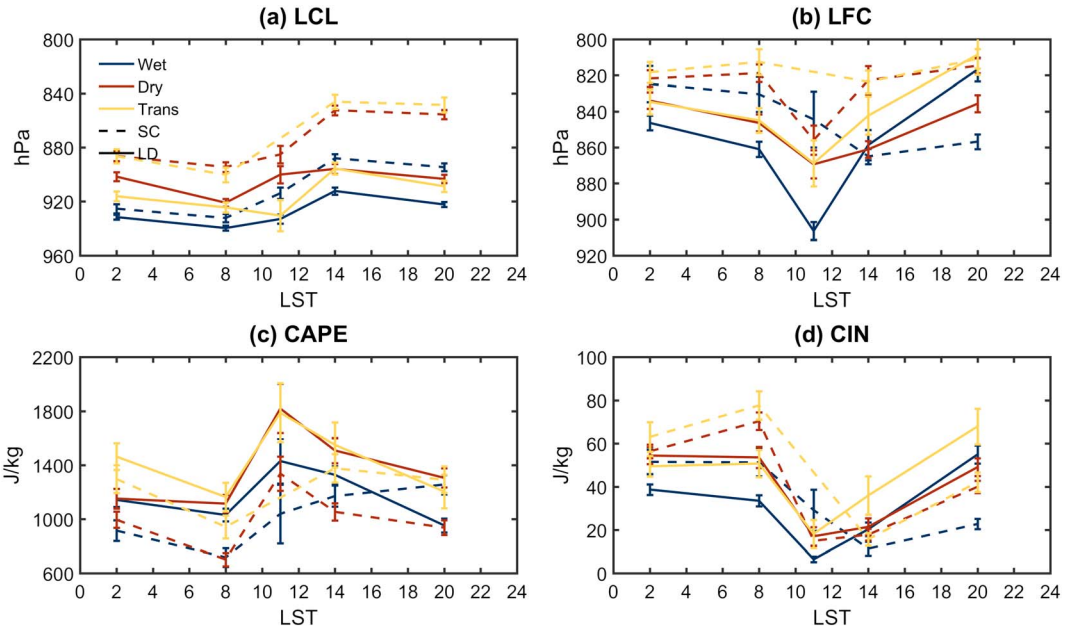

Figure 12. Average instability indices (LCL, LFC, CAPE, CIN) derived from rawinsonde data in SC and LD days during each season. The error bar represents 1 standard error.

pronounced at upper troposphere (above 9 km), indicating it could take hours for deep convection to moist the surrounding environment. In the dry season, RH and *q* are up to 20% and 1.8 g/kg higher, respectively, for LD days than for SC days in both lower and middle troposphere (~1–6 km) at 08 LST. At 14 and 20 LST, the largest increase of RH associated with LD relative to SC appears in the middle to upper troposphere (4–14 km), as expected from the convective detrainment of moisture in the upper troposphere. Such an increase of humidity is larger during the dry and transition seasons than during the wet season, possibly because a less saturated environment allows more moistening by the convective detrainment of water vapor or evaporation/sublimation of hydrometeors in convective anvils. During the transition season, LD days are generally wetter compared to SC days at nearly all tropospheric levels. The above analysis generally supports previous studies that found that a wetter layer in lower troposphere facilitates the transition from shallow to deep convection in other regions like SGP and tropical Indian Ocean [*Bretherton et al*., 2004; *Holloway and Neelin*, 2009; *Nuijens et al*., 2009; *Powell and Houze*, 2015; *Ruppert and Johnson*, 2015; *Zhang and Klein*, 2010]. However, the magnitude and depth of the wetness varies by season. As for the source of the lower tropospheric moisture increase in LD days, other than moisture convergence of the column, extensive early morning shallow clouds resulting from a higher ambient RH, could also contribute to moisten the lower and middle troposphere in the wet season. This could be implied by the collocated wetter level (Figure 10a) and increased cloud fraction in Figure 4d, but less likely so in the dry season as very few shallow convection is seen before 08 LST in Figure 4e.

5.3. Atmospheric Instability

In order to explore how the instability condition varies between SC and LD days during different seasons, composite equivalent potential temperature (θ_e) and saturation equivalent potential temperature (θ_{se}) profiles are plotted in Figure 11. For a rising parcel with average mixed layer temperature and specific humidity assuming the pseudoadiabatic process, its θ_e would be conservative as marked by the arrow in each subfigure. The level at which the straight line intersects with the θ_{se} line in the lower troposphere (pointed by arrowhead) represents the level of free convection (LFC); the level at which they intersect in the middle or upper troposphere (not shown in Figure 11) represents the equilibrium level (EL) or the limit of convection (LOC); the area enclosed by the θ_{se} profile and the straight dotted line (extension line of the arrow) between LFC and EL represents the CAPE. Additionally, specific mean values and standard errors of the lifting condensation level (LCL), LFC, CAPE, and CIN are also plotted in Figure 12. Note that the LCL in Figure 12a is conceptually similar to p_{LCL} in Figure 7, but they are calculated differently. Here the LCL is calculated from the 500 m

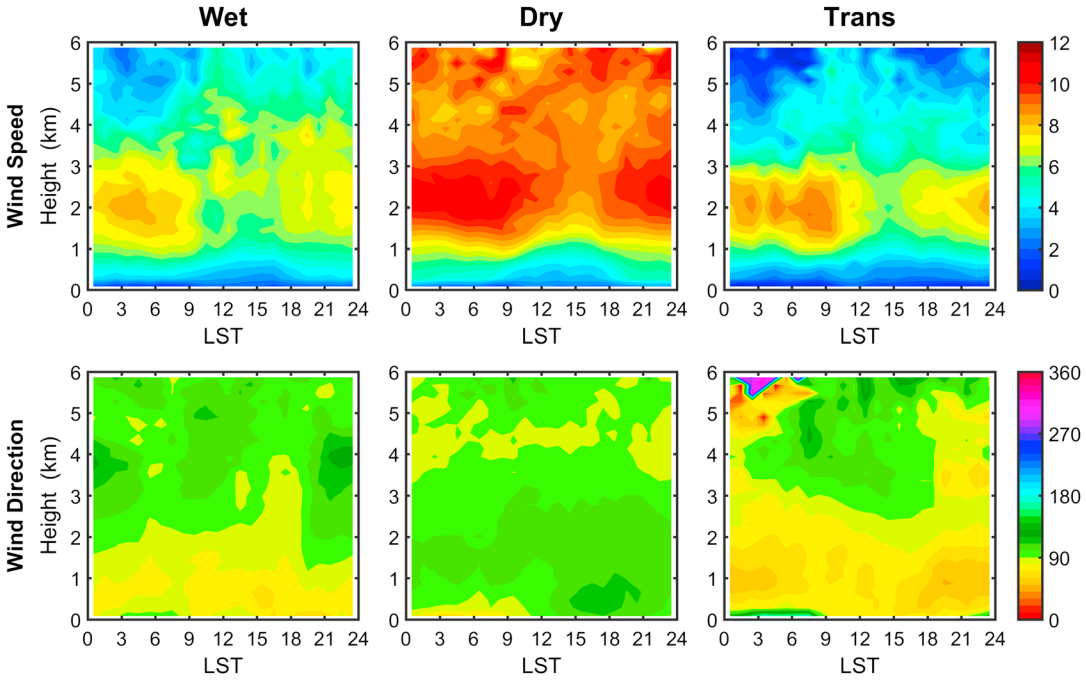

Figure 13. Composite diurnal cycle of wind speed and wind direction from the radar wind profiler during each season.

mixed layer temperature and specific humidity from rawinsonde data, while p_{LCL} is calculated using formula from *Betts et al*. [2002] with the temperature and RH from surface observations.

The comparison between SC and LD days during all three seasons demonstrates that LD is generally associated with a larger CAPE, smaller CIN, and lower LCL and LFC before the transition to deep convection (Figure 12). A lower LCL indicates a lower cloud base; a lower LFC requires less lift to initiate convection; a larger CAPE and smaller CIN can provide more buoyancy and less initial thermodynamic barrier to the development of deep convection. Figure 11 indicates that the boundary layer temperature (θ_{se}) in LD days increases slower than that in SC days, especially during the wet season. This is due to less solar heating at the surface caused by more cloud cover. The shallower daytime ABL would reduce dry air entrainment from the free troposphere, resulting in a more moist ABL with smaller CIN in LD days. Also, a larger boundary layer θ_e, due to the presence of more moisture, combined with a colder atmosphere lead to the higher CAPE in LD days.

During the LD days, LFC at 08 LST is about 1.5–1.7 km and does not vary much for different seasons as shown in Figure 11 (the wet season is slightly lower). However, at 11 LST, LFC drops more significantly during the wet season than during the other two seasons which can make shallow convection easier to initiate. This

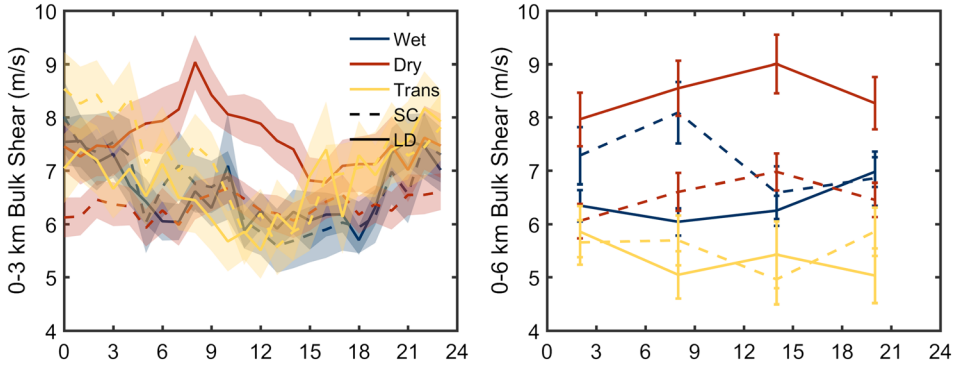

Figure 14. Composite (left) 0–3 km vertical wind shear (from radar wind profiler) and (right) 0–6 km vertical wind shear (from rawinsonde) in SC and LD days during each season. The shaded regions and error bars represent 1 standard error.

probably leads to more extensive shallow convection before the transition to deep convection in the wet season (Figure 4). Also, during the dry and transition seasons, the boundary layer temperature (θ_{se}) is higher, but the midtropospheric temperature is similar to that of the wet season. The resultant steeper temperature lapse rate could also be the cause that the LFC drops less than that during the wet season as the boundary layer θ_e increases. During the wet season, the occurrence of LD is associated with smaller CAPE and CIN than during the dry and transition seasons. This reduced CIN is largely because of the higher humidity within the ABL, resulting mainly from high humidity in the troposphere [*Fu et al*., 1999]. Although the transition season has the highest CAPE before the transition to deep convection, CAPE difference is less significant between SC and LD days than that during the other two seasons, indicating that it is a less important factor for the transition season at Manaus in the central Amazon.

5.4. Tropospheric Wind and Wind Shear

The composite diurnal cycle of wind speed and direction measured by the radar wind profiler (Figure 13) provides a relatively complete picture of the wind structure in the lower to midtroposphere and its seasonal variation. Note that the wind profiler only measures wind speed above 120 m, which does not include the surface level as shown in Figures 7e and 7f. The vertical structure of the horizontal wind field changes significantly from the wet to dry (or from dry to transition) season. During the wet (transition) seasons, the average wind speed maximum is ~8.5 (9.0) m/s; the wind direction is mostly NE (northeasterly) in the boundary layer and E (easterly) in the lower to midtroposphere. However, during the dry season, easterly winds prevail from boundary layer to the midtroposphere, and the average wind speed maximum increases to ~11.0 m/s. This directional difference in the lower tropospheric wind field can also account for the seasonal variation in moisture as northeasterly wind transports more humid air from the northern equatorial Atlantic which leads to an increase of convection over the Amazon [*Wang and Fu*, 2002].

The 0–3 km and 0–6 km bulk vertical wind shear (VWS_{0-3} and VWS_{0-6}) are contrasted for SC and LD days during each season in Figure 14. Note that VWS_{0-3} is calculated with the radar wind profiler data as in Figure 13, but VWS_{0-6} is computed using rawinsonde wind data since the wind observation in the midtroposphere from the profiler is not so reliable (a lot of missing data). During the dry season, both the VWS_{0-3} (Figure 14, left) and the VWS_{0-6} (Figure 14, right) for LD days are significantly larger than that for SC days. This larger shear is mostly due to its weak surface wind (Figure 7), especially in the early morning before convection initiates. However, there is no obvious distinction in the VWS_{0-3} between SC days and LD days during the wet and transition seasons. Furthermore, the wet and transition seasons also show weaker VWS_{0-6} in LD days than in SC days. Thus, while larger vertical wind shear may appear to link to the shallow-to-deep convection transition during the dry season, it may have no influence or suppress the shallow-to-deep convection transition during the wet and transition seasons.

6. Conclusions and Discussion

Using the combined measurement of the rain/cloud fraction from the SIPAM S band radar reflectivity and ARSCL product during the GOAmazon 2014/15 field campaign experiment, we characterized the diurnal cycle of rain/cloud fraction and precipitation with focus on the shallow-to-deep convection transition in the Central Amazon during the wet, dry and dry-to-wet transition seasons. SC cases are defined as the days when only shallow or congestus convection are observed without transition to deep convection during the daytime. For these SC cases, shallow convection are most extensive and longest lasting during the wet season, and they are the least extensive during the transition season. LD cases are defined as the days when the shallow-to-deep convection transition occurs during the daytime. For these LD cases, shallow convection is also most extensive during the wet season before its transition to deep convection, and the deep convection has the largest rain/cloud fraction and longest lasting diurnal peak rain rate. In contrast, the dry season has the latest diurnal peak rain rate due to a later transition to deep convection with the lowest rain/cloud fraction. However, the diurnal peak rain rate is as strong as that during the wet season. The rain rate and convection depth for LD cases are the greatest during the transition season. And its rapid shallow-to-deep convection transition leads to an early diurnal peak rain rate.

Environmental conditions possibly related to the shallow-to-deep convection transition are then analyzed based on the composite analysis for both SD and LD cases, including: surface meteorology, atmospheric humidity, atmospheric instability, and wind shear. Analysis of surface meteorology shows that the LD cases

Table 1. Environmental Preconditions (08-11 LST) Favorable for Shallow-to-Deep Convection Transition

	Surface Meteorology							Atmospheric Humidity		Atmospheric Instability				Vertical Wind Shear	
	$F_{SW\downarrow}$	$F_{LW\uparrow}$	T_s	q_s	V	H	LE	PWV	RH/q	LCL (hgt)	LFC (hgt)	CAPE	CIN	$VWS_{0\text{-}3}$	$VWS_{0\text{-}6}$
Wet	↓	↓	↓	↑	↓	↓	-	↑	↑ (low)	↓	↓	↑↑	↓	-	↓
Dry			↓↓	↑↑		↓↓		↑↑	↑(low-to-mid)	↓↓				↑	↑
Trans												↑		-	-

are generally associated with a lower surface temperature, higher surface humidity, shallower mixed layer, and smaller sensible heat flux and smaller surface wind speed. Except for the surface wind, these parameters are mostly in phase with the smaller downward solar radiation in LD days caused by more extensive cloud coverage. In addition, comparison of surface radiative and heat fluxes between observation and ECMWF-DIAG also show some discrepancies, which indicates that the energy balance and cloud amount representation in ECMWF model can be significantly different from that in nature and these differences of local fluxes in turn can lead to dramatic difference of cloud and rainfall between model and observation.

The LD cases are also related to larger PWV possibly due to large-scale moisture transport convergence. The wet season has the highest and least variable PWV while the dry season has the lowest PWV. Higher humidity before the transition to deep convection in LD days is consistent with the idea of lower tropospheric moistening as documented in previous works for the tropical ocean as listed in sections 1 and 5.2. However, moisture difference between SC and LD cases is not distinguishable at all levels for all seasons. Anomalously high moisture above 4 km seems to be not required for the development of LD during the wet season whereas during the dry and transition season, a deeper moist layer up to midtroposphere is presented before the transition to deep convection. As for atmosphere instability, a larger CAPE, smaller CIN, and lower LFC generally promote the transition to deep convection. This high instability precondition in LD days matches what is observed in SGP [*Zhang and Klein*, 2010], but this study shows that these instability variables and their statistical significances can still vary during different seasons. While CAPE is larger for LD cases than for SC cases during the wet and dry seasons, CAPE does not change significantly between SC and LD cases during the transition season. In general, the atmospheric instability conditions of the transition season are closer to that of the dry season in regard to a higher LFC, larger CIN, and larger CAPE than the wet season. However, the LCL and LFC for LD cases are as low as those during the wet season due to a stronger increase of humidity. This combination of high CAPE and CIN, along with a wetter environment than the dry season, enable the atmosphere to develop more intense convection. The dependence of the shallow-to-deep convection transition on the wind shear is not as clear as that for the moisture and instability parameters. A significant wind shear difference present during the dry season where a larger 0–3 km and 0–6 km bulk shear could be linked to the transition to deep convection. However, during the wet and transition season, the difference of shear condition between SC and LD days is not significant, and oppositely, wind shear for LD days is a little smaller than for SC.

Table 1 summarizes the anomalous conditions of the most environmental variables shown in Figures 6–14 which likely favor the shallow-to-deep convection transition, as indicated by the variable difference at 08–11 LST between LD and SC cases in each season. The time interval of 08–11 LST is selected, because the thermodynamic profile represented by the rawinsonde data at this time is a good predictor of thermodynamic conditions prior to the occurrence of deep convection in the late morning and early afternoon [*Fu et al.*, 1999]. For each column (variable), the hyphen symbol means insignificant LD/SC difference (1 standard error shades overlap), one arrow means significant, and two arrows mean more significant (only compared to the same column). Here note that the positive shortwave flux F_{SW} are downward while the positive longwave flux F_{LW} and sensible heat flux H and latent heat flux LE are upward. The upward arrows denote positive (increasing) anomalies, whereas the downward arrows indicate negative (decreasing) anomalies.

In summary, during the wet season, a more moist atmosphere due to prevailing northeasterly winds, strong moisture convergence, and frequent deep convection during both day and night promotes the occurrence of more extensive shallow convection and reduces solar radiation to the surface. This leads to a slower increase of ABL temperature before noon which makes LFC drop more and finally trigger the transition to more widespread but less intense deep convection with earlier onset and longer lasting rainfall. During the transition season, less shallow convection and more solar radiation lead to a quicker increase of ABL temperature

and a steeper lapse rate, which will help build up stronger CIN/CAPE, result in deep convection with stronger convective updrafts and peak rain rate. During the dry season, although instability conditions are very similar to those of the transition season, the drier environment resulting from both the circulation and less frequent convection would cause more dry entrainment and weaken and postpone the transition to deep convection.

This paper builds upon many previous works, provides detailed contrast of environmental parameters on SC/LD cases, and makes plausible explanations of their potential impacts on the shallow-to-deep convection transition. However, uncertainties still exist both in data and analysis methods. First, the rawinsonde profile at 08 LST is generally used to represent the condition before the shallow-to-deep convection transition as the transition is mostly observed around noon. However, the time of shallow convection occurrence and the transition time could vary from morning to late afternoon. Thus, the 08 LST profile may not be suitable for explaining those late transition cases. Second, the results about the relationship between the transition and its environmental controls are based on the SC/LD. This classification went through subjective processes like threshold determination of cloud/rain fraction and removal of nonlocally formed MCS cases. Because of the limited 2 year time range of the data and the definition of seasons and SC/LD cases, sample number varies a lot among different seasons and cases. For example, during the transition season, LD cases are much fewer and deep convection is stronger than other two seasons, so the diurnal cycle of rainfall and cloud/rain fraction could be more sensitive to case selection. Further research would require improvements on these issues. Our future work will focus on contrasting different tropical or subtropical ARM sites (e.g., Central Amazon, Tropical West Pacific, West Africa, and SGP) to see how environmental conditions impacting the shallow-to-deep convection transition vary over regions of different surface type and atmospheric circulation. Also, it may help scaling up the analysis using larger data sets like satellite observations (for convection and precipitation) and radio occultation measurements (for thermodynamic profiles) and reanalysis data.

Acknowledgments

This work was funded by the GOAmazon project under grants DE-SC0011117 and 2013/50538-7, which is supported jointly by the U.S. Department of Energy (DOE), the São Paulo Research Foundation (FAPESP), and the Amazonas Research Foundation (FAPEAM). The first author is also supported by the China Scholarship Council (CSC). All the data used in this study are available through the ARM data archive (http://www.archive.arm.gov); the ECMWF-DIAG data are only distributed to ARM sponsored scientists and their support staff and student, and retrieval of this data set will need a "site license" from the ARM program. The authors would like to thank Ashley Williamson for his help in accessing the ECMWF-DIAG data and Rachael Isphording for editing this manuscript. The authors are also grateful to the reviewers and Editor, all of whom provided helpful comments and suggestions that improved the manuscript.

References

Ackerman, T. P., and G. M. Stokes (2003), The Atmospheric Radiation Measurement program, *Phys. Today*, *56*(1), 38–44.

Anber, U., P. Gentine, S. G. Wang, and A. H. Sobel (2015), Fog and rain in the Amazon, *Proc. Natl. Acad. Sci. U.S.A.*, *112*(37), 11,473–11,477.

Betts, A., G. Fisch, C. Von Randow, M. A. F. Silva Dias, J. C. P. Cohen, R. Da Silva, and D. R. Fitzjarrald (2009), The Amazonian boundary layer and mesoscale circulations, in *Amazonia and Global Change*, edited by M. Keller et al., AGU, Washington, D. C., doi:10.1029/2008GM000720.

Betts, A. K. (2009), Land-Surface-Atmosphere Coupling in Observations and Models, *J. Adv. Model Earth Sy.*, *1*.

Betts, A. K., and M. A. F. S. Dias (2010), Progress in understanding land-surface-atmosphere coupling from LBA Research, *J. Adv. Model. Earth Syst.*, *2*, 6, doi:10.3894/JAMES.2010.2.6.

Betts, A. K., J. D. Fuentes, M. Garstang, and J. H. Ball (2002), Surface diurnal cycle and boundary layer structure over Rondonia during the rainy season, *J. Geophys. Res.*, *107*(D20), 8065, doi:10.1029/2001JD000356.

Bretherton, C. S., M. E. Peters, and L. E. Back (2004), Relationships between water vapor path and precipitation over the tropical oceans, *J. Clim.*, *17*(7), 1517–1528.

Cohen, J. C. P., D. R. Fitzjarrald, F. A. F. D'Oliveira, I. Saraiva, I. R. d. S. Barbosa, A. W. Gandu, and P. A. Kuhn (2014), Radar-observed spatial and temporal rainfall variability near the Tapajós-Amazon confluence, *Revista Brasileira de Meteorologia*, *29*(spe), 8, doi:10.1590/0102-778620130058.

Collow, A. B., V. P. Ghate, M. A. Miller, and L. C. Trabachino (2016), A one-year study of the diurnal cycle of meteorology, clouds and radiation in the West African Sahel region, *Q. J. R. Meteorol. Soc.*, *142*(694), 16–29.

Del Genio, A. D., Y. H. Chen, D. Kim, and M. S. Yao (2012), The MJO Transition from Shallow to Deep Convection in CloudSat/CALIPSO Data and GISS GCM Simulations, *J. Clim.*, *25*(11), 3755–3770.

Dias, M. A. F. S., et al. (2002), Cloud and rain processes in a biosphere-atmosphere interaction context in the Amazon Region, *J. Geophys. Res.*, *107*(D20), 8072, doi:10.1029/2001JD000335.

European Centre for Medium Range Weather Forecast (1994), The Description of the ECMWF/WCRP Level III—A Global Atmospheric Data Archive.

Foley, J. A., et al. (2007), Amazonia revealed: forest degradation and loss of ecosystem goods and services in the Amazon Basin, *Front. Ecol. Environ.*, *5*(1), 25–32.

Friedlingstein, P., et al. (2006), Climate-carbon cycle feedback analysis: Results from the (CMIP)-M-4 model intercomparison, *J. Clim.*, *19*(14), 3337–3353.

Friedlingstein, P., M. Meinshausen, V. K. Arora, C. D. Jones, A. Anav, S. K. Liddicoat, and R. Knutti (2014), Uncertainties in CMIP5 Climate Projections due to Carbon Cycle Feedbacks, *J. Clim.*, *27*(2), 511–526.

Fu, R., B. Zhu, and R. E. Dickinson (1999), How do atmosphere and land surface influence seasonal changes of convection in the tropical amazon?, *J. Clim.*, *12*(5), 1306–1321.

Gash, J. H. C., and C. A. Nobre (1997), Climatic Effects of Amazonian Deforestation: Some Results from ABRACOS, *Bull. Am. Meteorol. Soc.*, *78*(5), 823–830, doi:10.1175/1520-0477(1997)078<0823:CEOADS>2.0.CO;2.

Greco, S., R. Swap, M. Garstang, S. Ulanski, M. Shipham, R. C. Harriss, R. Talbot, M. O. Andreae, and P. Artaxo (1990), Rainfall and Surface Kinematic Conditions over Central Amazonia during Able-2b, *J. Geophys. Res.*, *95*(D10), 17,001–17,014, doi:10.1029/JD095iD10p17001.

Hagos, S., Z. Feng, K. Landu, and C. N. Long (2014), Advection, moistening, and shallow-to-deep convection transitions during the initiation and propagation of Madden-Julian Oscillation, *J. Adv. Model Earth Sy.*, *6*(3), 938–949.

Holloway, C. E., and J. D. Neelin (2009), Moisture Vertical Structure, Column Water Vapor, and Tropical Deep Convection, *J. Atmos. Sci.*, *66*(6), 1665–1683.

Khairoutdinov, M., and D. Randall (2006), High-resolution simulation of shallow-to-deep convection transition over land, *J. Atmos. Sci.*, *63*(12), 3421–3436.
Kodama, C., et al. (2015), A 20-Year Climatology of a NICAM AMIP-Type Simulation, *J. Meteorol. Soc. Jpn.*, *93*(4), 393–424.
Kollias, P., E. E. Clothiaux, M. A. Miller, E. P. Luke, K. L. Johnson, K. P. Moran, K. B. Widener, and B. A. Albrecht (2007), The Atmospheric Radiation Measurement Program cloud profiling radars: Second-generation sampling strategies, processing, and cloud data products, *J. Atmos. Oceanic Technol.*, *24*(7), 1199–1214.
Laurent, H., L. A. T. Machado, C. A. Morales, and L. Durieux (2002), Characteristics of the Amazonian mesoscale convective systems observed from satellite and radar during the WETAMC/LBA experiment, *J. Geophys. Res.*, *107*(D20), 8054, doi:10.1029/2001JD000337.
Li, W. H., R. Fu, and R. E. Dickinson (2006), Rainfall and its seasonality over the Amazon in the 21st century as assessed by the coupled models for the IPCC AR4, *J. Geophys. Res.*, *111*, D02111, doi:10.1029/2005JD006355.
Machado, L. A. T., et al. (2014), THE CHUVA PROJECT How Does Convection Vary across Brazil?, *Bull. Am. Meteorol. Soc.*, *95*(9), 1365–1380.
Machado, L. A. T., H. Laurent, N. Dessay, and I. Miranda (2004), Seasonal and diurnal variability of convection over the Amazonia: A comparison of different vegetation types and large scale forcing, *Theor. Appl. Climatol.*, *78*(1–3), 61–77.
Malhi, Y., and J. Grace (2000), Tropical forests and atmospheric carbon dioxide, *Trends Ecol. Evol.*, *15*(8), 332–337.
Marengo, J. A., L. M. Alves, W. R. Soares, D. A. Rodriguez, H. Camargo, M. P. Riveros, and A. D. Pablo (2013), Two Contrasting Severe Seasonal Extremes in Tropical South America in 2012: Flood in Amazonia and Drought in Northeast Brazil, *J. Clim.*, *26*(22), 9137–9154.
Marengo, J. A., and J. C. Espinoza (2016), Extreme seasonal droughts and floods in Amazonia: causes, trends and impacts, *Int. J. Climatol.*, *36*(3), 1033–1050.
Martin, S. T., et al. (2016), Introduction: Observations and Modeling of the Green Ocean Amazon (GoAmazon2014/5), *Atmos. Chem. Phys.*, *16*(8), 4785–4797.
Nuijens, L., B. Stevens, and A. P. Siebesma (2009), The Environment of Precipitating Shallow Cumulus Convection, *J. Atmos. Sci.*, *66*(7), 1962–1979.
Petersen, W. A., R. Fu, M. X. Chen, and R. Blakeslee (2006), Intraseasonal forcing of convection and lightning activity in the southern Amazon as a function of cross-equatorial flow, *J. Clim.*, *19*(13), 3180–3196.
Petersen, W. A., S. W. Nesbitt, R. J. Blakeslee, R. Cifelli, P. Hein, and S. A. Rutledge (2002), TRMM observations of intraseasonal variability in convective regimes over the Amazon, *J. Clim.*, *15*(11), 1278–1294.
Powell, S. W., and R. A. Houze (2015), Effect of dry large-scale vertical motions on initial MJO convective onset, *J. Geophys. Res. Atmos.*, *120*, 4783–4805, doi:10.1002/2014JD022961.
Rao, V. B., I. F. A. Cavalcanti, and K. Hada (1996), Annual variation of rainfall over Brazil and water vapor characteristics over South America, *J. Geophys. Res.*, *101*(D21), 26,539–26,551.
Rickenbach, T. M., R. N. Ferreira, J. B. Halverson, D. L. Herdies, and M. A. F. S. Dias (2002), Modulation of convection in the southwestern Amazon basin by extratropical stationary fronts, *J. Geophys. Res.*, *107*(D20), 8040, doi:10.1029/2000JD000263.
Rowe, A. K., and R. A. Houze (2015), Cloud organization and growth during the transition from suppressed to active MJO conditions, *J. Geophys. Res. Atmos.*, *120*, 10,324–10,350, doi:10.1002/2014JD022948.
Ruppert, J. H. (2016), Diurnal timescale feedbacks in the tropical cumulus regime, *J. Adv. Model Earth Sy.*, *8*(3), 1483–1500, doi:10.1002/2016MS000713.
Ruppert, J. H., and R. H. Johnson (2015), Diurnally Modulated Cumulus Moistening in the Preonset Stage of the Madden-Julian Oscillation during DYNAMO, *J. Atmos. Sci.*, *72*(4), 1622–1647.
Ruppert, J. H., and R. H. Johnson (2016), On the cumulus diurnal cycle over the tropical warm pool, *J. Adv. Model Earth Sy.*, *8*(2), 669–690.
Sobel, A. H. (2003), On the coexistence of an evaporation minimum and precipitation maximum in the warm pool, *J. Clim.*, *16*(6), 1003–1009.
Stokes, G. M., and S. E. Schwartz (1994), The Atmospheric Radiation—Measurement (Arm) Program—Programmatic Background and Design of the Cloud and Radiation Test-Bed, *Bull. Am. Meteorol. Soc.*, *75*(7), 1201–1221.
Tokay, A., and D. A. Short (1996), Evidence from tropical raindrop spectra of the origin of rain from stratiform versus convective clouds, *J. Appl. Meteorol.*, *35*(3), 355–371.
Vera, C., G. Silvestri, B. Liebmann, and P. Gonzalez (2006), Climate change scenarios for seasonal precipitation in South America from IPCC-AR4 models, *Geophys. Res. Lett.*, *33*, L13707, doi:10.1029/2006GL025759.
Wang, H., and R. Fu (2002), Cross-equatorial flow and seasonal cycle of precipitation over South America, *J. Clim.*, *15*(13), 1591–1608.
Wei, J. F., H. Su, and Z. L. Yang (2016), Impact of moisture flux convergence and soil moisture on precipitation: a case study for the southern United States with implications for the globe, *Clim. Dyn.*, *46*(1–2), 467–481.
Williams, E., et al. (2002), Contrasting convective regimes over the Amazon: Implications for cloud electrification, *J. Geophys. Res.*, *107*(D20), 8082, doi:10.1029/2001JD000380.
Xu, W. X., and S. A. Rutledge (2016), Time scales of shallow-to-deep convective transition associated with the onset of Madden-Julian Oscillations, *Geophys. Res. Lett.*, *43*, 2880–2888, doi:10.1002/2016GL068269.
Yin, L., R. Fu, E. Shevliakova, and R. E. Dickinson (2013), How well can CMIP5 simulate precipitation and its controlling processes over tropical South America?, *Clim. Dyn.*, *41*(11–12), 3127–3143.
Zhang, G. J., and N. A. Mcfarlane (1995), Sensitivity of Climate Simulations to the Parameterization of Cumulus Convection in the Canadian Climate Center General-Circulation Model, *Atmos. Ocean*, *33*(3), 407–446.
Zhang, Y. Y., and S. A. Klein (2010), Mechanisms Affecting the Transition from Shallow to Deep Convection over Land: Inferences from Observations of the Diurnal Cycle Collected at the ARM Southern Great Plains Site, *J. Atmos. Sci.*, *67*(9), 2943–2959.